

# Temperature-dependent cycling performance and ageing mechanisms of

## $C_6/LiNi_{1/3}Mn_{1/3}Co_{1/3}O_2$ batteries

Dongjiang Li<sup>a,b</sup>, Hu Li<sup>a</sup>, Dmitri Danilov<sup>b,c</sup>, Lu Gao<sup>d</sup>, Jiang Zhou<sup>e</sup>, Rüdiger-A. Eichel<sup>b,f</sup>,

Yong Yang<sup>a,\*</sup> and Peter H. L. Notten<sup>b,c,d,g,\*</sup>

<sup>a</sup> State Key Lab for Physical Chemistry of Solid Surfaces, College of Chemistry and Chemical Engineering, Xiamen University, Xiamen, 361005, China

<sup>b</sup> Forschungszentrum Jülich, Fundamental Electrochemistry (IEK-9), D-52425 Jülich, Germany

<sup>c</sup> Department of Electrical Engineering, Eindhoven University of Technology,  
Eindhoven, 5600 MB, The Netherlands

<sup>d</sup> Department of Chemical Engineering and Chemistry, Eindhoven University of Technology,  
Eindhoven, 5600 MB, The Netherlands

<sup>e</sup> Tianjin Lishen Battery Joint-stock Co., Ltd., Tianjin, 300384, China

<sup>f</sup> RWTH Aachen University, D-52074 Aachen, Germany

<sup>g</sup> University of Technology Sydney, Broadway, Sydney, NSW 2007, Australia

\* Corresponding authors:

Yong Yang and Peter H. L. Notten

Tel: +86-592-2185753

Postal address: 361005 Xiamen

Email address: [yyang@xmu.edu.cn](mailto:yyang@xmu.edu.cn) (Yong Yang) and [p.h.l.notten@tue.nl](mailto:p.h.l.notten@tue.nl) (Peter Notten)



## Abstract

Ageing mechanisms of NMC-based Li-ion ( $C_6/LiNi_{1/3}Mn_{1/3}Co_{1/3}O_2$ ) batteries have been investigated under various cycling conditions. The electromotive force (EMF) curves are regularly determined by mathematical extrapolation of voltage discharge curves. The irreversible capacity losses determined from the EMF curves have been investigated as a function of time and cycle number. Parasitic side reactions, occurring at the cathode and anode, are considered to be responsible for charge-discharge efficiency (CDE) and discharge-charge efficiency (DCE), respectively. The recently developed non-destructive voltage analysis method is also applied to the present battery chemistry. The decline of the second plateau of the  $dV_{EMF}/dQ$  curves upon cycling is considered to be an indicator of graphite degradation whereas the development of the third peak in these derivative curves is considered to be an indicator for electrode voltage slippage. XPS measurements confirm the deposition of transition-metal elements at the graphite electrode, indicating dissolution of these metals from the cathode. Furthermore, XPS analyses confirm the existence of a Cathode-Electrolyte-Interface (CEI) layer. The outer CEI layer is composed of various compounds, such as carbonate-related Li salts, LiF and  $NiF_2$ , *etc.*, while the inner CEI layer is dominantly composed of fluoride-related compounds, such as  $NiF_2$ . Finally, a cathode degradation model including transition-metal dissolution and structure transformation is proposed.

**Key words:** Layered-oxid Cathode materials; Solid-Electrolyte-Interface; Cathode-Electrolyte-Interface; Capacity loss; Electromotive force; Derivative voltage analysis

## Highlights:

- EMF curves are regularly determined during cycling.
- Charging efficiency of both the anode and cathode is investigated.
- Individual electrode degradation is investigated by  $dV_{EMF}/dQ$ .
- Cathode dissolution is confirmed by XPS analyses at the anode.
- Composition of CEI layer is investigated by XPS analyses.

## 1. Introduction

The demand for large-scale rechargeable batteries in the application of electric vehicles and smart grids has been growing rapidly in the past few years. Higher energy density combined with long cycle life and high safety is one of the key requirements in these applications. Lithium nickel-manganese-cobalt oxide (NMC) cathode material is considered to be a promising candidate for high-energy-density batteries, due to their larger theoretical specific capacity ( $\approx 260 \text{ mAh}\cdot\text{g}^{-1}$ ) compared to olivine ( $\text{LiFePO}_4$ ,  $160 \text{ mAh}\cdot\text{g}^{-1}$ ) or spinel materials ( $\text{LiMn}_2\text{O}_4$ ,  $150 \text{ mAh}\cdot\text{g}^{-1}$ ) [1-3].

The ternary NMC electrode system contains a large group of family members, including  $\text{LiNi}_{1/3}\text{Co}_{1/3}\text{Mn}_{1/3}\text{O}_2$  (NMC(111)),  $\text{LiNi}_{0.5}\text{Co}_{0.2}\text{Mn}_{0.3}\text{O}_2$  (NMC(532)),  $\text{LiNi}_{0.6}\text{Co}_{0.2}\text{Mn}_{0.2}\text{O}_2$  (NMC(622)),  $\text{LiNi}_{0.425}\text{Co}_{0.15}\text{Mn}_{0.425}\text{O}_2$ ,  $\text{LiNi}_{0.25}\text{Co}_{0.5}\text{Mn}_{0.25}\text{O}_2$ , *etc.* These compounds commonly have a layered structure, which is similar to that of  $\text{LiCoO}_2$  [4]. Electronic structure studies have shown that NMC consists of  $\text{Ni}^{2+}$ ,  $\text{Mn}^{4+}$  and  $\text{Co}^{3+}$  in the as-made materials [5-8].  $\text{Ni}^{2+}$  will be oxidized to  $\text{Ni}^{4+}$  during the initial stages of charging, while  $\text{Co}^{3+}$  will be oxidized to  $\text{Co}^{4+}$  in the higher voltage range.  $\text{Mn}^{4+}$  remains inactive throughout normal charging and provides structural stability. The NMC electrode has a similar or higher achievable specific capacity compared to  $\text{LiCoO}_2$  when cycled in the potential window of 2.5 to 4.3 V. Advantageously, the cycling ability of the NMC electrode is better than that for  $\text{LiCoO}_2$  due to its higher thermal stability [9, 10].

A lot of research has been carried out to investigate the degradation mechanisms of NMC batteries [11-23]. Generally, Li immobilization in the Solid-Electrolyte-Interface (SEI) at the graphite electrode is considered to be the main origin of the battery capacity losses [24-29]. The cathode material decay becomes significant under severe aging conditions, *e.g.* at high temperature, using high (dis)charge currents and upon overcharging [30-33]. The degradation mechanism of NMC electrode is still under discussion. It is well known that the NMC material experiences a phase transition from the rhombohedral space group  $R\bar{3}m$  (initial “O3” phase) to the monoclinic space group  $C2/m$  (“O1” phase) when the charge voltage is beyond 4.4 V vs  $\text{Li}^+/\text{Li}$  [14]. The “O1”  $\text{Li}_y\text{Ni}_{1/3}\text{Co}_{1/3}\text{Mn}_{1/3}\text{O}_2$  phase has been clearly observed at  $y \approx 0.3$  [34]. Cycling above this phase transition voltage ( $> 4.4 \text{ V}$ ) will lead to a faster capacity decay of the cathode. High currents [9] and voltages [1] are believed to be more detrimental to cause such distortion at the surface of these materials. Metal dissolution from the NMC electrode in acidic solutions ( $\text{LiPF}_6$  based electrolytes)

and at high temperatures has also been reported [35-40]. Metal dissolution occurs at various State-of-Charge (SoC) and is therefore considered a common degradation phenomenon.

In the present work, the aging mechanisms of NMC(111) batteries under various cycling currents and temperatures have been investigated. The loss of maximum capacities, as determined from extrapolated EMF curves, are discussed. Graphite degradation and electrode voltage slippage are unraveled by voltage derivative analyses. Cathode dissolution and subsequent metal ion deposition at the anode is confirmed by XPS analyses. Moreover, the composition of the Cathode-Electrolyte-Interface (CEI) layer formed at the cathode is investigated by XPS.

## 2. Experimental

### 2.1 Cycling experiments

For the cycling experiments a set of cylindrical NMC (ANR18650) 2.2 Ah Li-ion batteries has been investigated. The electrochemical experiments were carried out with a Maccor automatic cycling equipment. The batteries, subjected to the cycling experiments, were kept in climate chambers in order to control the temperature at 40 and 60°C.

Before conducting the cycling experiments all batteries were activated for 5 cycles and characterization cycles were subsequently carried out at 40 and 60°C, corresponding to the cycling temperatures, in order to derive the electromotive force (EMF) curves. During characterization all batteries were charged in the constant-current constant-voltage (CCCV) mode. A 0.5 C charging rate was used in the CC-mode followed by CV charging at 4.2 V during 1 hours. The batteries were then discharged at various constant currents (0.1, 0.2, 0.3, 0.5 and 1.0 C-rates) in the subsequent cycles, using a cut-off voltage of 3.0 V. On the basis of these sets of discharge curves, the EMF was extracted by mathematical extrapolation. Details of the EMF estimation can be found in our previous publications [27, 29, 41-43].

After the characterization process has been completed all batteries were cycled under various conditions summarized in Table 1. The second column shows the various (dis)charging currents and the last column shows the duration of each cycle. Since the cycling time of each cycle is strongly dependent on the current, the duration of each cycle varies in different experiments. Note that the actual duration of each cycle for a given discharge current is also varying due to the decreasing battery capacity upon cycling, as is indicated by the duration range indicated in Table 1. All batteries were regularly re-characterized after approximately every 20 days.

**Table 1.** Cycling conditions of the NMC batteries.

	Temperature		Duration of each cycle (hours)
	40°C	60°C	
(dis)charging current	0.1	0.1	25~22
(C-rate)	0.3	0.3	8.2~7.1
	0.5	0.5	5.4~4.0
	1.0	1.0	3.3~3.9

## 2.2 XPS measurements

In order to investigate the degradation mechanisms of both the anode and cathode upon cycling, X-ray Photoelectron Spectroscopy (XPS) have been carried out on both the graphite and NMC electrodes, dismantled from the batteries after cycling under the various conditions. The batteries were fully discharged at a 0.5 C-rate before opening in an Argon glove box, and small pieces of the electrodes were cut and rinsed by pure solvent (Dimethyl Carbonate). The samples were transferred to the XPS equipment in a closed container in order to reduce the influence of moisture and air. XPS analyses were carried out on a Quantum 2000 ESCA spectrometer (Physical Electronics, USA), using an Al  $K_{\alpha}$  monochromatic irradiation (1486.6 eV) at a working pressure smaller than  $7 \cdot 10^{-8}$  bar. Depth profiling was carried out, using Ar ion-beam sputtering with 500 eV. The sputtering rate was equivalent to 0.26 nm/s on Ta<sub>2</sub>O<sub>5</sub>.

## 3. Results and discussion

The NMC batteries have been cycled at various currents at 40 and 60°C. Fig. 1a shows an example of a set of characterization curves at 60°C and corresponding extrapolated EMF curve. Fig. 1b shows an example of the development of the voltage discharge curves upon cycling at 60°C. Both the capacity and voltage plateaus decrease upon cycling, indicating a decline of the discharge storage capacity and voltage degradation. Fig. 1c shows the corresponding extrapolated EMF curves at the indicated cycle numbers. Similar to the discharge curves, a contraction of the EMF curves upon cycling is also observed. Obviously, the voltage plateaus in the EMF curves are more distinguishable and at higher voltage levels than in the discharging curves, due to the overpotential contribution under current flowing conditions.

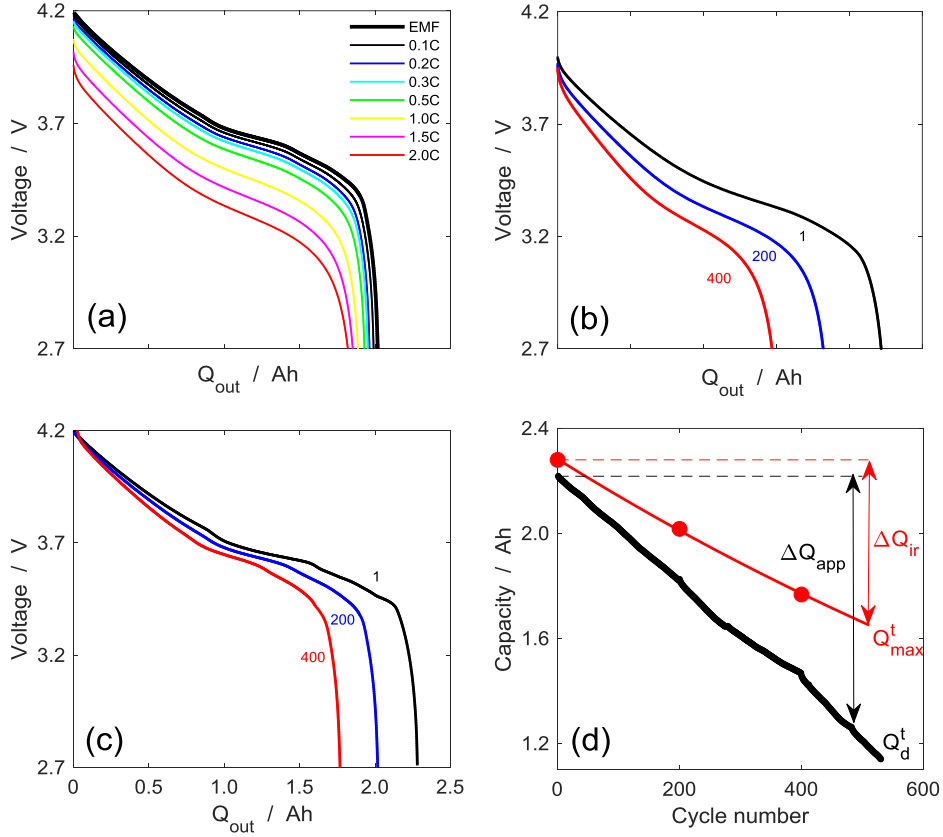


**Fig. 1.** Voltage discharge characterization curves and the extrapolated EMF curve (a). Examples of the development of voltage discharge curves upon cycling (b) and corresponding extrapolated EMF curves (c). (d) The as-measured ( $I = 2C$ ) discharge capacity ( $Q_d^t$ ) and extrapolated maximum storage capacity ( $Q_{max}^t$ ) at a given time ( $t$ ) of the NMC(111) battery as a function of cycle number.  $\Delta Q_{ir}$  and  $\Delta Q_{app}$  represent the as-defined (Eqs. 1-2) irreversible capacity loss and apparent capacity loss, respectively.

The capacities extracted from both the discharge curves and EMF curves are defined as the discharge capacity ( $Q_d^t$ ) and maximum storage capacity ( $Q_{max}^t$ ), respectively. Fig. 1d shows the development of  $Q_d^t$  (black curve) and  $Q_{max}^t$  (red curve) as a function of cycle number. In line with the conclusion obtained from Figs. 1a and b,  $Q_{max}^t$  is always larger than  $Q_d^t$ . The apparent capacity loss is calculated from

$$\Delta Q_{app} = Q_d^0 - Q_d^t, \quad (1)$$

and the irreversible capacity loss is calculated from

$$\Delta Q_{ir} = Q_{max}^0 - Q_{max}^t \quad (2)$$

Obviously, the development of  $\Delta Q_{ir}$  is less significant than that of  $\Delta Q_{app}$ .  $\Delta Q_{app}$  includes the irreversible capacity loss and the capacity loss due to the battery polarization, *i.e.* impedance losses. The polarization (overpotential) of the battery is clearly influenced by the cycle number. More and more cyclable  $\text{Li}^+$  ions cannot be extracted when the overpotential increases due to kinetic limitations. Therefore, only the irreversible capacity loss  $\Delta Q_{ir}$  is considered to be the “real” capacity loss in this work.

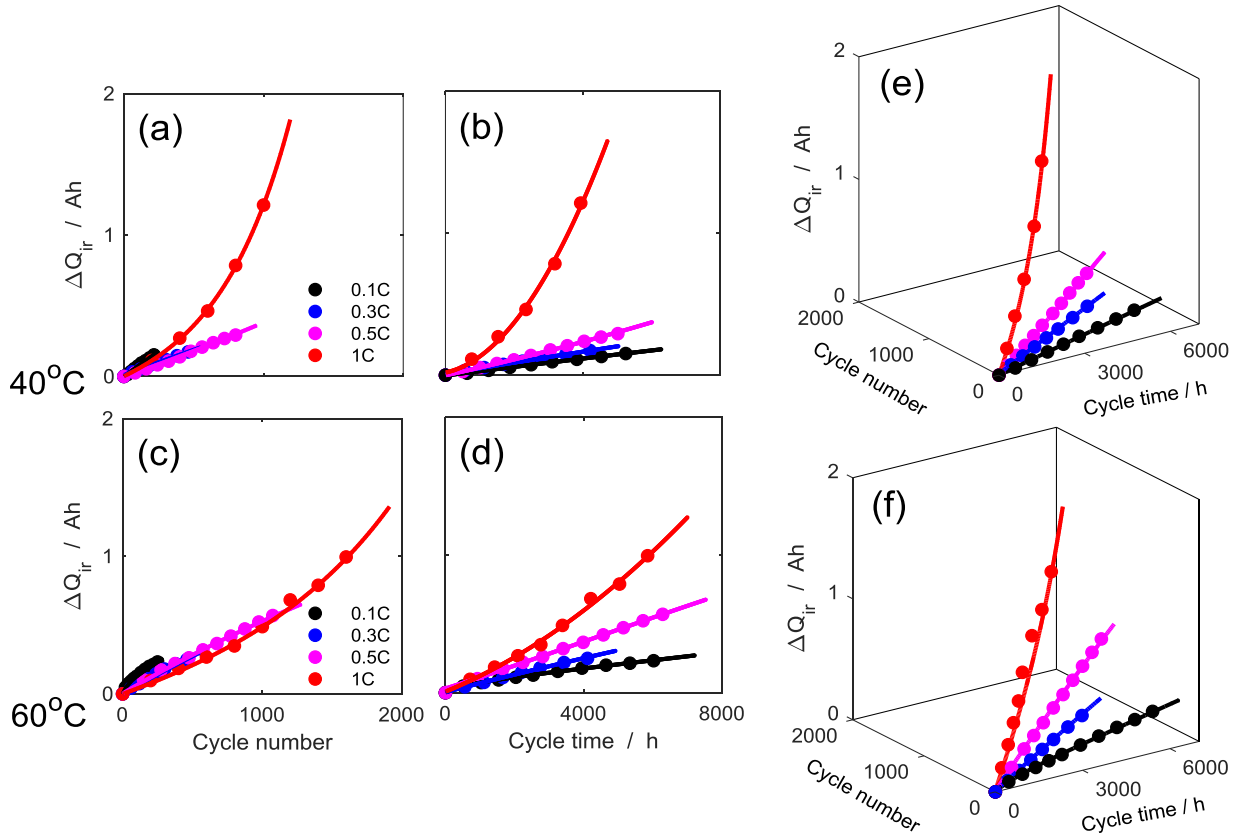


**Fig. 2.** The development of  $\Delta Q_{ir}$  at various cycling currents as a function of cycle number ((a) and (c)) and cycle time ((b) and (d)) at 40 and 60°C. 3D representation of  $\Delta Q_{ir}$  at 40 °C (e) and 60°C (f).

Figs. 2a-d show the development of  $\Delta Q_{ir}$  of batteries cycled at the various indicated C-rates at 40 and 60°C as a function of cycle number and time. When  $\Delta Q_{ir}$  is plotted as a function of cycle number (Figs. 2a and c), the irreversible capacity loss at a certain cycle number increases with decreasing current (apart from the 1 C-rate results in Fig. 2a). However, when  $\Delta Q_{ir}$  is plotted as a

function of time (Figs. 2b and d), the irreversible capacity loss at a given cycling time increases with increasing current. These results indicate that both the cycle number and time influence the irreversible capacity loss.

In order to illustrate the individual contributions of cycle number and time on  $\Delta Q_{ir}$ , the 3D plotting approach proposed before has also been adopted in this case. Figs. 2e and f show the development of  $\Delta Q_{ir}$  as a function of both cycle number and time at 40 and 60°C, respectively. The development of  $\Delta Q_{ir}$  in these two plots is very similar to the case of LFP batteries which has been discussed in detail before [29]. The dependency on the cycle number is attributed to the cycling effect, inducing electrode volume fluctuations, thereby generating cracks in the SEI layers covering the graphite electrode. The SEI formation in these cracks additionally leads to irreversible capacity losses observed. The dependency on time is attributed to the continuous SEI growth on the SEI-covered graphite surface. The irreversible capacity loss caused by this part of SEI formation depends only on time. A more detailed description to distinguish between the individual contributions of cycle number and time can be found in ref. [29].

Apart from current, temperature is considered to be another important parameter which certainly influences the capacity loss. It can be seen from Fig. 2d that  $\Delta Q_{ir}$  is higher at 60°C when the cycling current is low, *i.e.* in the range of 0.1 to 0.5 C-rate. However, when the cycling current increases to 1 C,  $\Delta Q_{ir}$  becomes larger at 40°C.

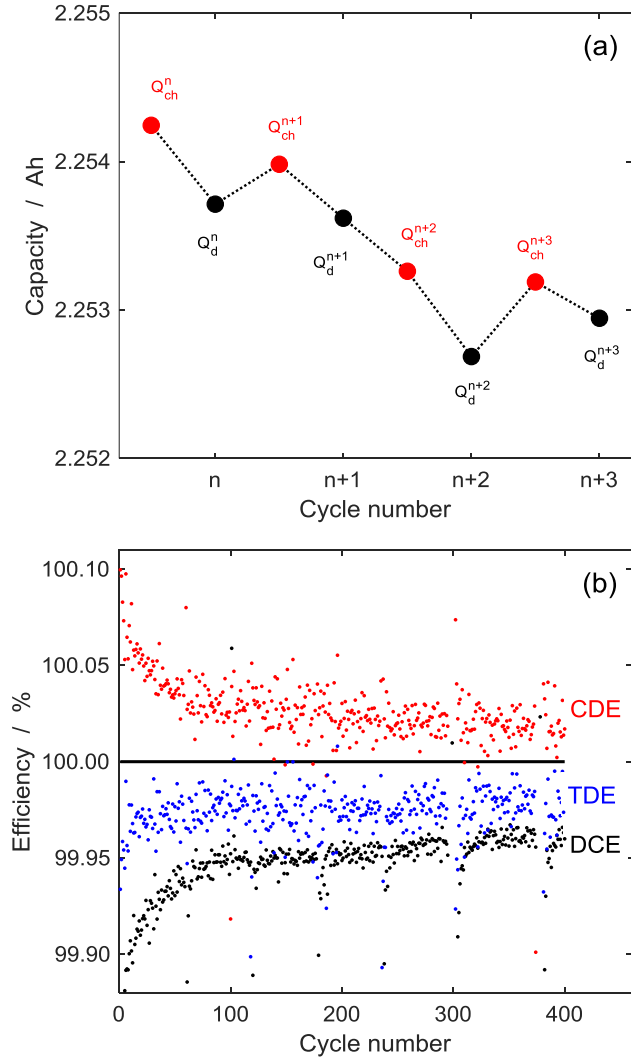


**Fig. 3.** (a) Charging ( $Q_{ch}^n$ ) and discharging capacity ( $Q_d^n$ ) as a function of cycle number, referring in this example to 0.1 C-rate and 40°C. (b) Development of the discharge-charge efficiency (DCE), charge-discharge efficiency (CDE) and total discharge efficiency (TDE) as a function of cycle number at 0.3 C-rate at 60°C.

Fig. 3a shows an example of the development of the charging capacity ( $Q_{ch}^n$ ) and the discharging capacity ( $Q_d^n$ ) as a function of cycle number at 0.1 C-rate and 40°C. It can strikingly be seen that  $Q_d^n$  is always smaller than  $Q_{ch}^n$  while  $Q_{ch}^{n+1}$  is fluctuating around  $Q_d^n$ .  $Q_{ch}^n$  represents the total amount of charge transferred from the cathode to the anode during charging, while  $Q_d^n$  represents the total amount of charge that can be extracted from the anode and transported to the cathode during discharging. The subsequent charging capacity ( $Q_{ch}^{n+1}$ ) denotes the amount of

charge that can be re-extracted from cathode and transported to the anode during the subsequent charging process. Ideally,  $Q_{ch}^n = Q_d^n = Q_{ch}^{n+1}$ . However, under real operating conditions a small part of the  $\text{Li}^+$  ions are immobilized by the SEI formation process during intercalation into the graphite electrode. Therefore, the amount of cyclable  $\text{Li}^+$  ions extracted from the anode during the subsequent discharging ( $Q_d^n$ ) is always smaller than  $Q_{ch}^n$ . There are two possibilities to explain the fluctuation of  $Q_{ch}^{n+1}$  around  $Q_d^n$ . One explanation is that the internal resistance of the battery system is not stable, leading to fluctuating overpotentials, which influences the final charging cut-off current during the constant-voltage charging period. Another reason might be that there are some parasitic side reactions, *e.g.* electrolyte oxidation, which generate electrons at the cathode, leading to an increase of  $Q_{ch}^{n+1}$ .

In order to get a more in-depth understanding of the charging efficiency, three parameters DCE, CDE and TDE are proposed. DCE is the discharge-charge efficiency, defined as the ratio between the discharge and charge capacities in the same cycle

$$DCE = \frac{Q_d^n}{Q_{ch}^n}. \quad (3)$$

Traditionally, DCE is denoted as the coulombic efficiency. On the other hand, CDE is the charge-discharge efficiency, defined as the ratio between the charge capacity and the discharge capacity in the previous cycle

$$CDE = \frac{Q_{ch}^{n+1}}{Q_d^n}. \quad (4)$$

The development of DCE and CDE is determined by the side-reactions at the anode and cathode, respectively. The total discharge efficiency (TDE) is defined as

$$TDE = \frac{Q_d^{n+1}}{Q_d^n}. \quad (5)$$

Fig. 3b shows the development of DCE, CDE and TDE as a function of cycle number at 0.3 C-rate at 60°C. Obviously, DCE is always smaller than 100%, indicating that the parasitic side reaction which is related to the  $\text{Li}^+$  ion immobilization on the anode during charging. In contrast, CDE is, in most cases, larger than 100%, indicating that the processes occurring at the cathode, *e.g.*, oxidation of the electrolyte, can release more charge during the charging [44]. Interestingly, CDE is approaching 100% after long-term cycling, implying that the system becomes stable and

the parasitic side reactions at the cathode are suppressed. TDE is also smaller than 100%, indicating that the overall discharge capacity decreases as a function of cycle number.

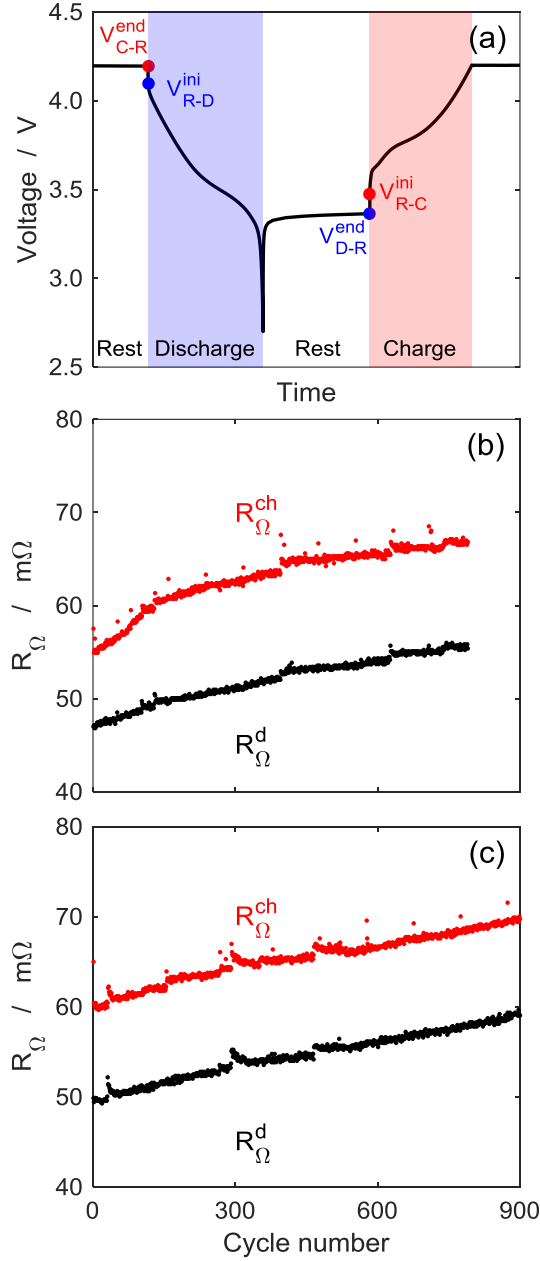


**Fig. 4.** (a) Definition of the battery voltage at various stages of the (dis)charging process:  $V_{C-R}^{end}$  is the voltage the end of the resting period after charging, and  $V_{R-D}^{ini}$  is the voltage at the initial stage of discharging after resting.  $V_{D-R}^{end}$  represents the battery voltage at the end of the resting period after discharging, and  $V_{R-C}^{ini}$  is the initial battery voltage during charging after resting. The development of the as-calculated ohmic

resistance during charging ( $R_{\Omega}^{ch}$ ) and discharging ( $R_{\Omega}^d$ ) as a function of cycle number at 0.5 C-rate at 40°C (b) and 60°C (c).

The parasitic reactions occurred at the anode and cathode lead to a series of disadvantages, *e.g.*, overpotential development, resistance increase, electrode capacity decay, *etc.* Fig. 4a shows the definitions of the voltage-related terminologies in a complete cycle.  $V_{C-R}^{end}$  represents the battery voltage at the end of the resting period after charging but just before the discharging step is commenced (the last point of the resting period),  $V_{R-D}^{ini}$  is the battery voltage at the moment the discharging step is initiated after resting (the first point of discharging),  $V_{D-R}^{end}$  denotes the battery voltage at the end of the resting period after discharging, and  $V_{R-C}^{ini}$  is the initial battery voltage during charging.  $V_{C-R}^{end}$  and  $V_{D-R}^{end}$  indicate the equilibrium state of the battery after charging and discharging, respectively.  $V_{R-D}^{ini}$  and  $V_{R-C}^{ini}$  reflect the initial overpotential of the discharging and charging processes, respectively.

The difference between  $V_{D-R}^{end}$  and  $V_{R-C}^{ini}$  ( $\eta_{ch} = V_{R-C}^{ini} - V_{D-R}^{end}$ ),  $V_{C-R}^{end}$  and  $V_{R-D}^{ini}$  ( $\eta_d = V_{R-D}^{ini} - V_{C-R}^{end}$ ), determines the overpotentials of the charging and discharging processes, respectively. Since the time interval between  $V_{D-R}^{end}$  and  $V_{R-C}^{ini}$ ,  $V_{C-R}^{end}$  and  $V_{R-D}^{ini}$  is sufficiently small, the corresponding ohmic resistance during charging ( $R_{\Omega}^{ch}$ ) and discharging ( $R_{\Omega}^d$ ) can be calculated on the basis of these overpotentials and the (dis)charge currents. Fig. 4b shows the development of the charging ( $R_{\Omega}^{ch}$ ) and discharging ( $R_{\Omega}^d$ ) ohmic resistance upon cycling at 0.5 C-rate at 40°C. It can be seen that both  $R_{\Omega}^{ch}$  and  $R_{\Omega}^d$  increase as a function of cycle number. Strikingly,  $R_{\Omega}^{ch}$  is found to be larger than  $R_{\Omega}^d$  in all cases, indicating that the battery polarization during charging is larger than that during discharging. Fig. 4c shows the development of  $R_{\Omega}^{ch}$  and  $R_{\Omega}^d$  upon cycling at 0.5 C-rate at 60°C. Similar to the case shown in Fig. 4b, both  $R_{\Omega}^{ch}$  and  $R_{\Omega}^d$  increase with cycle number.

Fig. 5 shows the development of  $-dV_{EMF}/dQ$  versus  $Q_{out}$  curves as a function of indicated cycle numbers at 0.1, 0.3 and 0.5 C-rate at 40°C and 60°C. Three distinct peaks are observed which are indicated as  $\alpha$  (gray),  $\beta$  (blue) and  $\gamma$  (red). The slopes and peaks in the  $dV_{EMF}/dQ$  curves are corresponding to the slopes in the EMF curves while depressions in  $dV_{EMF}/dQ$  curves correspond to the plateaus in the EMF curves. In order to facilitate the analysis of the shift of these peaks, all curves are aligned with respect to  $\alpha$  peak at approximately 0.9 Ah. The blue vertical lines indicate the position of  $\alpha$  and  $\beta$  peak in the pristine state. The red sloping lines connect the  $\beta$  peak of the

various  $dV_{EMF}/dQ$  curves in order to make the shift of the  $\beta$  peak more visible. It can be seen that the shift of the  $\beta$  peak is negligible at low current (0.1C) at both 40 and 60°C. This shift at 60°C becomes more pronounced when the current increases to 0.5C. Obvious changes of the  $\gamma$  peak upon cycling is observed in Figs. 5c and f. It can be seen that the  $\gamma$  peak becomes indistinct upon cycling to almost disappear after 500 cycles.

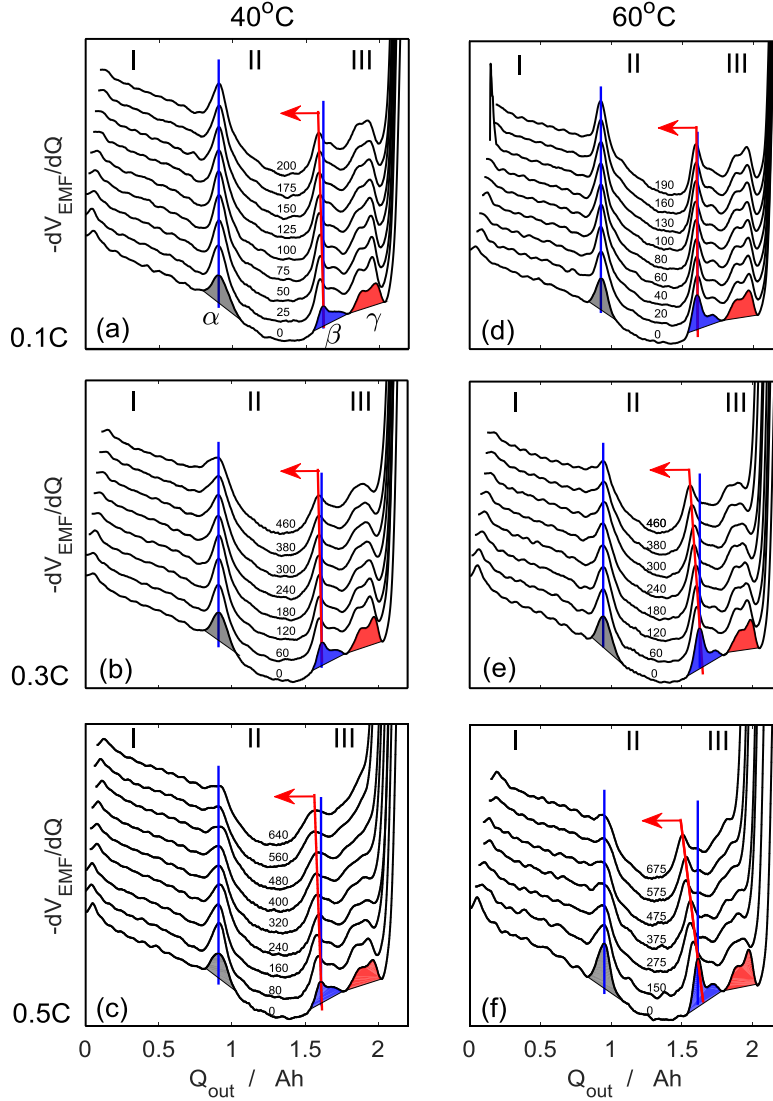


**Fig. 5.** The development of  $-dV_{EMF}/dQ$  versus  $Q_{out}$  curves as a function of indicated cycle number at various cycling currents at 40°C (a-c) and 60°C (d-f). The three distinct peaks are indicated as  $\alpha$  (gray),  $\beta$  (blue) and  $\gamma$  (red).

A novel nondestructive approach to analyze the graphite degradation on the basis of  $dV_{EMF}/dQ$  curves has recently been developed and applied for the investigation of the ageing process of  $\text{LiFePO}_4$ -based Li-ion batteries [45]. In the present work this interesting approach is also applied to the present NMC chemistry. According to this approach, the peaks and depressions in the  $dV_{EMF}/dQ$  curves can be attributed to the slopes and plateaus of the graphite electrode potential. The shift of the  $\beta$  peak with respect to  $\alpha$  reflection indicates the degradation of the graphite electrode during cycling [39, 40]. Summarizing the above results it can be concluded that the graphite electrode degradation at  $60^\circ\text{C}$  is more severe than at  $40^\circ\text{C}$ , especially at higher currents. The change of the  $\gamma$  peak is attributed to the voltage slippage of the individual electrodes [46]. It can be concluded from Figs. 5c and f that both the anode and cathode degrade upon cycling at high currents (0.5C) at both 40 and  $60^\circ\text{C}$ . In order to unravel the detailed degradation mechanisms of the electrodes materials, postmortem XPS analyses have been carried out at both electrodes.

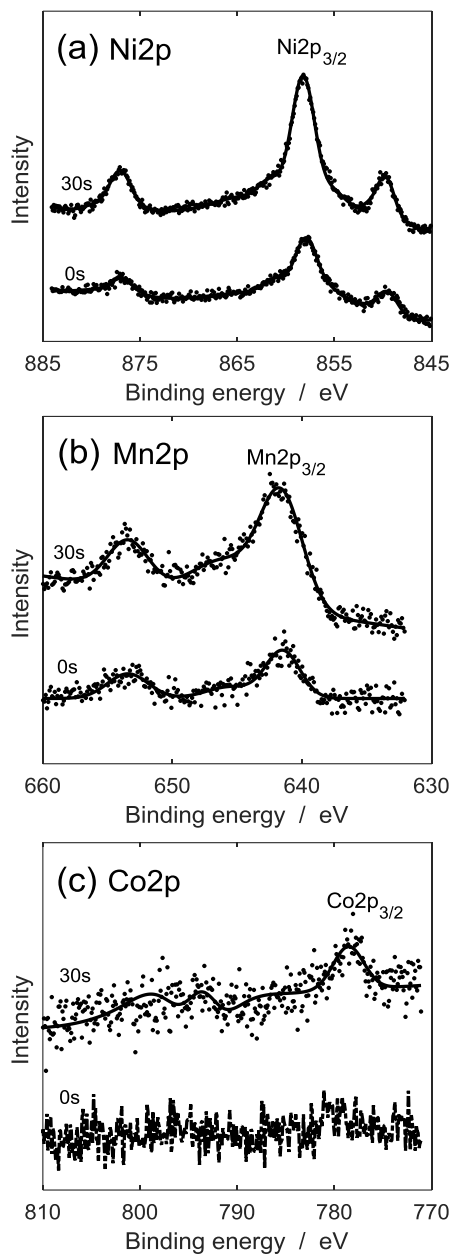


**Fig. 6.** The Ni2p (a), Mn2p (b) and Co2p (c) spectra of the aged graphite surface and after 30 s sputtering. The battery was cycled with 0.5C at 60°C.

Fig. 6 shows the evolution of the Ni2p (a), Mn2p (b) and Co2p (c) spectra of the dismantled graphite electrode (cycled with 0.5C at 60°C) after sputtering time  $t = 0$  and 30 s. The signal for Ni 2p<sub>3/2</sub> (a) and Mn 2p<sub>3/2</sub> (b) can be clearly observed at the aged graphite surface ( $t = 0$  s). The intensity of the Ni 2p<sub>3/2</sub> and Mn 2p<sub>3/2</sub> signal becomes even more significant after sputtering 30 s,

indicating that both elements are concentrated in the bulk of the SEI layers. In contrast with Ni and Mn, the signal of Co is hardly observed either at surface or after sputtering. The deposition of transition metal ions at the anode will lead to blockage of the graphite layered structure and finally lead to a decline of the accessible anode storage capacity. Moreover, the observation that transition metal elements are present at the anode demonstrates that these chemical elements are dissolved from the cathode after ageing under severe conditions.

Fig. 7a shows the evolution of the Ni2p spectra of the dismantled cathode electrode at two different sputtering times ( $t = 0$  and 30s). At the cathode surface (sputtering time  $t = 0$  s), two main peaks at 858.5 eV and 877.5 eV are clearly observed. The first peak at 858.5 eV is far deviated from the Ni2p<sub>3/2</sub> core peak of the lattice-Ni<sup>2+</sup> (854.7 eV) or Ni<sup>3+</sup> (856.3 eV), but very close to the Ni2p<sub>3/2</sub> core line of NiF<sub>2</sub> reported in ref. [47]. The rest peak at 877.5 eV is corresponding to the Ni2p<sub>1/2</sub> core level of NiF<sub>2</sub> compound. After sputtering 30 s, a wide shoulder peak at 855.3 eV appears beside the NiF<sub>2</sub> main peak. This shoulder peak is considered to be a composite signal of the lattice- Ni<sup>2+</sup> and Ni<sup>3+</sup>.

Fig. 7b shows the evolution of the Mn2p spectra of the cathode at the two indicated sputtering times. At the cathode surface at sputtering time  $t = 0$  s the signal of Mn2p is hardly observed. However, the intensity of Mn2p signal becomes very obvious after sputtering for 30 s. The binding energies at 642 eV and 653.5 eV in the spectra are attributed to the Mn 2p<sub>3/2</sub> and Mn 2p<sub>1/2</sub> core levels of Mn<sup>4+</sup> in the lattice structure. Mn remains inactive when the charging voltage is not extremely high, *i.e.* > 4.4V, therefore the valence state of Mn remains constant in the active cathode material.

Fig. 7c shows the evolution of the Co2p spectra of the cathode at both indicated sputtering times. Similarly to the case of the Mn2p spectra, Co2p is also invisible at the cathode surface at  $t = 0$  s. After sputtering 30 s, a sharp peak at 780 eV appears, which is assigned to the Co 2p<sub>3/2</sub> core line. The satellite reflection appearing at 786.6 eV is considered to be a fingerprint indication of the Co<sup>3+</sup> ion [48].

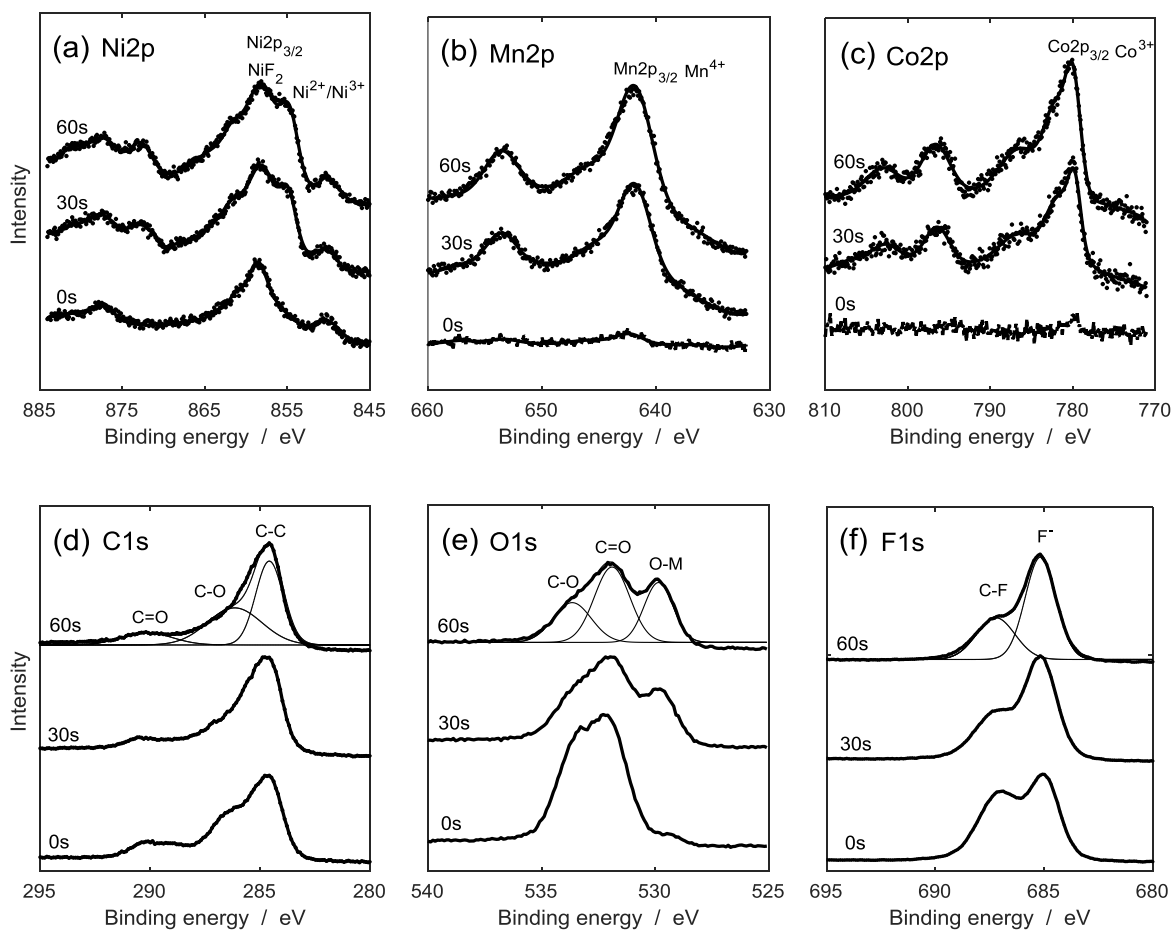


**Fig. 7.** The Ni2p (a), Mn2p (b), Co2p (c), C1s (d), O1s (e), F1s (f) spectra of the aged cathode electrode at various indicated sputtering time  $t = 0, 30, 60$  s.

It can be concluded from the Ni2p spectra discussed in Fig. 7a that NiF<sub>2</sub> has been formed at the cathode surface. The formation of NiF<sub>2</sub> is considered to be the result of the interaction between the electrolyte and the active material. It is also possible that Ni<sup>2+</sup> dissolves from the surface of the cathode material into the electrolyte and then re-precipitates at the electrodes surface in the form of NiF<sub>2</sub>. The deposited NiF<sub>2</sub> species can form a layer with a considerable thickness at the cathode, therefore, the signal of the transition metals (Ni, Co, Mn) in the lattice structure cannot be detected. The spectra of Mn2p and Co2p discussed in Figs. 7b and 7c, respectively, further confirm the existence of a passivation layer at the cathode surface. The formation of NiF<sub>2</sub> may lead to cathode structure deformation. Moreover, the passivation layer, also known as the cathode-electrolyte-interface (CEI) layer, can significantly influence the performance of Li-ion batteries, *e.g.* reduce

the cathode electrode capacity, enhance the battery polarization, retard the kinetics and lead to resistance increase, *etc.*

Electrolyte decomposition at the cathode may also contribute to the growth of the CEI layer. In order to have a more in-depth understanding of the composition of the CEI layer, the C1s, O1s and F1s spectra are also analyzed. Fig. 7d shows the development of C1s spectra at various indicated sputtering times. For the reason of clarity, only the curve at  $t = 60$  s is deconvoluted. The peak at 284.6 eV is attributed to the  $\underline{\text{C}}-\text{C}$  bond in carbon black. The peak at 286.1 eV is attributed to the  $\underline{\text{C}}-\text{O}$  bond and that at 290.3 eV is attributed to  $\underline{\text{C}}=\text{O}$ . The intensities of the  $\underline{\text{C}}-\text{O}$  and  $\underline{\text{C}}=\text{O}$  peaks decrease with respect to the intensity of the  $\underline{\text{C}}-\text{C}$  peak upon sputtering. However, the intensities of these three components are still considerably high after sputtering 60 s due to the porous nature of the cathode.

Fig. 7e shows the development of the O1s reflection of the aged cathode at various indicated sputtering times. Based on the intrinsic binding energies, three different O atoms have been identified. The peak at 529.9 eV is attributed to the lattice O ( $\underline{\text{O}}-\text{M}$ ) in the cathode material, the peak at 532 eV is attributed to  $\text{C}=\underline{\text{O}}$  and that at 533.6 eV is attributed to  $\underline{\text{O}}-\text{C}=\text{O}$ . The peak intensity of  $\text{C}=\underline{\text{O}}$  and  $\underline{\text{O}}-\text{C}=\text{O}$  is very strong at the cathode surface while the signal of lattice O ( $\underline{\text{O}}-\text{M}$ ) is completely invisible. After sputtering, some part of the surface components, *e.g.*  $\text{Li}_2\text{CO}_3$  and other electrolyte decomposition products, are removed. Consequently, the intensity of the  $\text{C}=\underline{\text{O}}$  and  $\underline{\text{O}}-\text{C}=\text{O}$  reflections decrease. Meanwhile, more and more O ( $\underline{\text{O}}-\text{M}$ ) is exposed to the surface, and the intensity of ( $\underline{\text{O}}-\text{M}$ ) peak therefore rapidly increases. Combining the discussion of Fig. 7d and 8b, it can be concluded that the carbonate-related Li salts are part of the CEI layer.

Fig. 7f shows the evolution of F1s spectra of the aged cathode. Obviously, two different F atoms can be identified in the spectra. The peak at 685.2 eV is attributed to  $\text{F}^-$  and that at 687.3 eV is attributed to  $\text{C}-\underline{\text{F}}$ . The intensity of  $\text{C}-\underline{\text{F}}$  peak decreases with increasing sputtering time, however, no significant intensity change is observed for  $\text{F}^-$  after sputtering.  $\text{C}-\underline{\text{F}}$  is considered to originate from the binder (PVdF) and the  $\text{F}^-$  anion is attributed to  $\text{NiF}_2$  and/or  $\text{LiF}$  compounds. The intensity decline of the  $\text{C}-\underline{\text{F}}$  peak can be explained by the decrease of the binder after sputtering. However, the amount of  $\text{F}^-$  anion seems to be increased after sputtering since the intensity of  $\text{F}^-$  slightly enhanced with respect to the  $\text{C}-\underline{\text{F}}$  peak. This striking phenomena indicates that the distribution of  $\text{F}^-$  anions (*i.e.*  $\text{NiF}_2$ ) is preferably located close to the active materials.

In general, the degradation mechanisms of NMC electrodes are different from those of the LFP electrodes investigated before [27, 29, 49]. The LFP electrode is generally considered to be stable at moderate temperature ( $< 40^{\circ}\text{C}$ ) and metal dissolution process only occurs significantly at elevated temperatures (*e.g.* at  $60^{\circ}\text{C}$ ). The NMC electrode degradation is, however, more complicated. Apart from metal dissolution, metal ion re-precipitation is another competitive process, which may occur at the cathode. Fig. 8 illustrates the main degradation mechanisms of NMC electrodes.

Similar to LFP batteries, Li salt decomposition is facilitated by the existence of residual water in the electrolyte (Fig. 8a). The corresponding chemical reactions can be described by



The formed HF will be dissociated into  $\text{H}^+$  and  $\text{F}^-$ , according to



As shown by Fig. 8b, the bonds of O-Li and O-M ( $\text{M} = \text{Ni}, \text{Co}, \text{Mn}$ ) collapse after frequent attacks of proton ions. The released O anion will immediately combine with  $\text{H}^+$  due to the high affinity of the O atom for  $\text{H}^+$  ions, forming water. Simultaneously, the transition metal cation is liberated and released to electrolyte, leading to electrode dissolution. These processes can be represented by

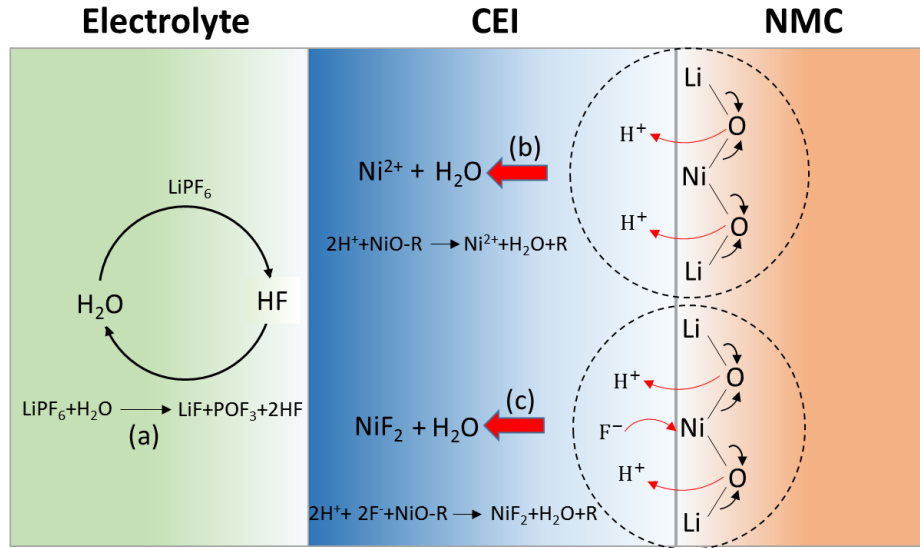
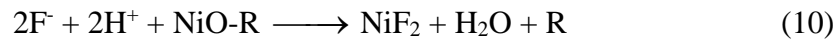


**Fig. 8.** Degradation mechanisms of NMC cathode materials. (a) denotes Li-salt decomposition in the electrolyte; (b) illustrates an example of Ni dissolution and (c) represents Ni re-precipitation at the cathode surface.



where R represents the residual composition of the host material. The dissolved Ni cations can be further transferred to the anode and subsequently reduced and deposited at the anode surface, which has been confirmed by the XPS analyses of Fig. 6.

When the concentration of  $\text{F}^-$  anions is sufficiently high,  $\text{Ni}^{2+}$  ions can also be precipitated onto the cathode surface by combining with  $\text{F}^-$  anions, thereby forming the so-called Cathode-Electrolyte-Interface (CEI) layer. The  $\text{NiF}_2$  deposition reaction is schematically shown by Fig. 8c. This precipitation reaction can simultaneously occur with the dissolution processes (b). This combined dissolution and precipitation reaction can be represented by



It can be concluded from both Fig. 8b and c that  $\text{H}^+$  is the driving force, leading to cathode degradation. The concentration of  $\text{H}^+$  is, however, not influenced by the cathode degradation

reactions (Eqs. 9 and 10) since the formed water can be converted into  $H^+$  again by the Li-salt decomposition reactions (Eqs. 6-8). Therefore, the residual water in the electrolyte can be considered to be an auto-catalyst for cathode degradation. In contrast,  $F^-$  ions are consumed in the course of both Fig. 8a and c, which leads to the consumption of  $PF_6^-$  ions and, consequently, to electrolyte degradation due to replacement of  $LiPF_6$  by  $LiF$  and  $POF_3$ . Apparently the newly formed CEI is not significantly resistive to the diffusion of  $H^+$  and  $F^-$  ions at the surface of the cathode material.

It is worthwhile to note that there are also some other side-reactions occurring at the cathode, such as the oxidation of electrolyte components, which lead to the formation of carbonate-related compounds. These compounds are also observed by the XPS analyses shown in Figs. 7d-f. Moreover, these oxidation reactions allow the cathode to gain extra electrons during the charging processes [44], which lead to CDE larger than 100%.

## 4 Conclusions

The EMF curves of NMC(111) batteries have been regularly determined by mathematical extrapolation of the measured voltage discharge curves. The maximum storage capacities, which have been accurately determined from the EMF curves, have been systematically investigated as a function of time and cycle number at various cycling currents and temperatures. It is found that the capacity loss increases with temperature and current. The charge-discharge efficiency is always found larger than 100% while discharge-charge efficiency is lower than 100% in the present NMC system. Parasitic side-reactions, occurring at the cathode and anode, are considered to be responsible for the behavior of these efficiencies. Those parasitic reactions strongly influence the battery overpotential, the resistance and the individual electrode storage capacities.

The  $dV_{EMF}/dQ$  curves calculated from the corresponding EMF curves have been investigated.  $dV_{EMF}/dQ$  analysis provides an efficient way to accurately determine the individual electrode capacity degradation. The changes of the peaks observed from the  $dV_{EMF}/dQ$  curves can be used to determine the anode material decay and voltage slippage effect.

Transition metal dissolution and structure transformation are considered to be the main cathode degradation mechanisms. The XPS analyses on the anode have confirmed the deposition of transition-metal elements, such as Ni and Mn at the graphite electrode, indicating dissolution of these chemical elements from the cathode. Furthermore, XPS analyses of the cathode have

confirmed the existence of the CEI layer. The outer CEI layer is composed of various compounds, such as carbonate-related Li salts, LiF and NiF<sub>2</sub>, *etc.*, while the inner CEI layer is preferably composed of fluoride-related compounds, such as NiF<sub>2</sub>.

## **Acknowledgements**

The authors appreciate the financial support from the Horizon 2020 program of the European Union under the grant of the AutoDrive project ‘Advancing fail-aware, fail-safe, and fail-operational electronic components, systems, and architectures for fully automated driving to make future mobility safer, affordable, and end-user acceptable’ (Grant No. 737469), the DEMOBASE project (Grant No. 769900) and the grant from the Science and Technology Office, Fujian Province (Grant No. 2014HZ0002-1).

## References

- [1] S.K. Jung, H. Gwon, J. Hong, K.Y. Park, D.H. Seo, H. Kim, J. Hyun, W. Yang, K. Kang, *Adv Energy Mater*, 4 (2014).
- [2] N. Yabuuchi, K. Yoshii, S.T. Myung, I. Nakai, S. Komaba, *J Am Chem Soc*, 133 (2011) 4404-4419.
- [3] K. Amine, Z.H. Chen, Z. Zhang, J. Liu, W.Q. Lu, Y. Qin, J. Lu, L. Curtis, Y.K. Sun, *J Mater Chem*, 21 (2011) 17754-17759.
- [4] X.L. Wang, K. An, L. Cai, Z.L. Feng, S.E. Nagler, C. Daniel, K.J. Rhodes, A.D. Stoica, H.D. Skorpenske, C.D. Liang, W. Zhang, J. Kim, Y. Qi, S.J. Harris, *Sci Rep-Uk*, 2 (2012).
- [5] B.J. Hwang, Y.W. Tsai, D. Carlier, G. Ceder, *Chem Mater*, 15 (2003) 3676-3682.
- [6] Y. Koyama, I. Tanaka, H. Adachi, Y. Makimura, T. Ohzuku, *J Power Sources*, 119 (2003) 644-648.
- [7] R. Robert, C. Villevieille, P. Novak, *J Mater Chem A*, 2 (2014) 8589-8598.
- [8] J. Choi, A. Manthiram, *J Electrochem Soc*, 152 (2005) A1714-A1718.
- [9] Y.B. He, F. Ning, Q.H. Yang, Q.S. Song, B.H. Li, F.Y. Su, H.D. Du, Z.Y. Tang, F.Y. Kang, *J Power Sources*, 196 (2011) 10322-10327.
- [10] N. Kiziltas-Yavuz, M. Herklotz, A.M. Hashem, H.M. Abuzeid, B. Schwarz, H. Ehrenberg, A. Mauger, C.M. Julien, *Electrochim Acta*, 113 (2013) 313-321.
- [11] D. Mohanty, H. Gabrisch, *J Power Sources*, 220 (2012) 405-412.
- [12] B.P. Matadi, S. Genies, A. Delaille, C. Chabrol, E. de Vito, M. Bardet, J.F. Martin, L. Daniel, Y. Bultel, *J Electrochem Soc*, 164 (2017) A2374-A2389.
- [13] J.A. Gilbert, J. Baren, T. Spila, S.E. Trask, D.J. Miller, B.J. Polzin, A.N. Jansen, D.P. Abraham, *J Electrochem Soc*, 164 (2017) A6054-A6065.
- [14] H. Gabrisch, R. Yazami, *Electrochem Solid St*, 13 (2010) A88-A90.
- [15] C. Zhan, J. Lu, A.J. Kropf, T.P. Wu, A.N. Jansen, Y.K. Sun, X.P. Qiu, K. Amine, *Nat Commun*, 4 (2013).
- [16] I. Belharouak, W.Q. Lu, D. Vissers, K. Amine, *Electrochem Commun*, 8 (2006) 329-335.
- [17] T. Schwieters, M. Evertz, M. Mense, M. Winter, S. Nowak, *J Power Sources*, 356 (2017) 47-55.
- [18] I. Buchberger, S. Seidlmayer, A. Pokharel, M. Piana, J. Hattendorff, P. Kudejova, R. Gilles, H.A. Gasteiger, *J Electrochem Soc*, 162 (2015) A2737-A2746.
- [19] B. Ziv, V. Borgel, D. Aurbach, J.H. Kim, X.C. Xiao, B.R. Powell, *J Electrochem Soc*, 161 (2014) A1672-A1680.
- [20] T. Yoshida, M. Takahashi, S. Morikawa, C. Ihara, H. Katsukawa, T. Shiratsuchi, J. Yamaki, *J Electrochem Soc*, 153 (2006) A576-A582.
- [21] D. Aurbach, B. Markovsky, M.D. Levi, E. Levi, A. Schechter, M. Moshkovich, Y. Cohen, *J Power Sources*, 81 (1999) 95-111.
- [22] B. Xu, C.R. Fell, M.F. Chi, Y.S. Meng, *Energ Environ Sci*, 4 (2011) 2223-2233.
- [23] A.N. Mansour, D.G. Kwabi, R.A. Quinlan, Y.C. Lu, S.H. Yang, *J Electrochem Soc*, 163 (2016) A2911-A2918.
- [24] B. Stiaszny, J.C. Ziegler, E.E. Krauss, J.P. Schmidt, E. Ivers-Tiffée, *J Power Sources*, 251 (2014) 439-450.
- [25] B. Stiaszny, J.C. Ziegler, E.E. Krauss, M.J. Zhang, J.P. Schmidt, E. Ivers-Tiffée, *J Power Sources*, 258 (2014) 61-75.
- [26] D.J. Li, D. Danilov, Z.R. Zhang, H.X. Chen, Y. Yang, P.H.L. Notten, *J Electrochem Soc*, 162 (2015) A858-A869.
- [27] D.J. Li, D.L. Danilov, J. Xie, L. Raijmakers, L. Gao, Y. Yang, P.H.L. Notten, *Electrochim Acta*, 190 (2016) 1124-1133.
- [28] Y. Kobayashi, T. Kobayashi, K. Shono, Y. Ohno, Y. Mita, H. Miyashiro, *J Electrochem Soc*, 160 (2013) A1415-A1420.
- [29] D.J. Li, D.L. Danilov, L. Gao, Y. Yang, P.H.L. Notten, *Electrochim Acta*, 210 (2016) 445-455.

- [30] H. Gabrisch, T.H. Yi, R. Yazami, *Electrochem Solid St*, 11 (2008) A119-A124.
- [31] J. Shu, R. Ma, L.Y. Shao, M. Shui, K.G. Wu, M.M. Lao, D.J. Wang, N.B. Long, Y.L. Ren, *J Power Sources*, 245 (2014) 7-18.
- [32] J. Shim, R. Kostecki, T. Richardson, X. Song, K.A. Striebel, *J Power Sources*, 112 (2002) 222-230.
- [33] A. Vu, L.K. Walker, J. Bareno, A.K. Burrell, I. Bloom, *J Power Sources*, 280 (2015) 155-158.
- [34] S.C. Yin, Y.H. Rho, I. Swainson, L.F. Nazar, *Chem Mater*, 18 (2006) 1901-1910.
- [35] D.R. Gallus, R. Schmitz, R. Wagner, B. Hoffmann, S. Nowak, I. Cekic-Laskovic, R.W. Schmitz, M. Winter, *Electrochim Acta*, 134 (2014) 393-398.
- [36] D. Aurbach, B. Markovsky, G. Salitra, E. Markevich, Y. Talyossef, M. Koltypin, L. Nazar, B. Ellis, D. Kovacheva, *J Power Sources*, 165 (2007) 491-499.
- [37] M. Ochida, Y. Domi, T. Doi, S. Tsubouchi, H. Nakagawa, T. Yamanaka, T. Abe, Z. Ogumi, *J Electrochem Soc*, 159 (2012) A961-A966.
- [38] J.L. Esbenshade, A.A. Gewirth, *Journal of the Electrochemical Society*, 161 (2014) A513-A518.
- [39] T. Joshi, K. Eom, G. Yushin, T.F. Fuller, *J Electrochem Soc*, 161 (2014) A1915-A1921.
- [40] H. Takahara, Y. Kobayashi, K. Shono, H. Kobayashi, M. Shikano, T. Nakamura, *Journal of the Electrochemical Society*, 161 (2014) A1716-A1722.
- [41] V. Pop, H.J. Bergveld, J.H.G. Op het Veld, P.P.L. Regtien, D. Danilov, P.H.L. Notten, *J Electrochem Soc*, 153 (2006) A2013-A2022.
- [42] H.J. Bergveld, W.S. Kruijt, P.H.L. Notten, *Battery management systems, design by modeling*, Kluwer Academic Publishers, Boston, 2002.
- [43] D. Danilov, R.A.H. Niessen, P.H.L. Notten, *J Electrochem Soc*, 158 (2011) A215-A222.
- [44] J.G. Xu, R.D. Deshpande, J. Pan, Y.T. Cheng, V.S. Battaglia, *J Electrochem Soc*, 162 (2015) A2026-A2035.
- [45] D.J. Li, D.L. Danilov, L. Gao, Y. Yang, P.H.L. Notten, *J Electrochem Soc*, 163 (2016) A3016-A3021.
- [46] A.J. Smith, J.C. Burns, J.R. Dahn, *Electrochem Solid St*, 14 (2011) A39-A41.
- [47] A.P. Grosvenor, M.C. Biesinger, R.S. Smart, N.S. McIntyre, *Surf Sci*, 600 (2006) 1771-1779.
- [48] Z. Chen, J. Wang, D.L. Chao, T. Baikie, L.Y. Bai, S. Chen, Y.L. Zhao, T.C. Sum, J.Y. Lin, Z.X. Shen, *Sci Rep-Uk*, 6 (2016).
- [49] D. Li, D. Danilov, B. Zwickirsch, M. Fichtner, Y. Yang, R.-A. Eichel, P.H.L. Notten, *J Power Sources*, (2018) 106-117.